Research Letter DOI: 10.15541/jim20230433

Mo/S Co-doped Graphene for Ammonia Synthesis: a Density Functional Theory Study

LI Honglan[1], ZHANG Junmiao[1], SONG Erhong[2], YANG Xinglin[1]

(1. School of Energy and Power Engineering, Jiangsu University of Science and Technology, Zhenjiang 212003, China; 2. State Key Laboratory of High Performance Ceramics and Superfine Microstructure, Shanghai Institute of Ceramics, Chinese Academy of Sciences, Shanghai 200050, China)

Abstract: In the industrial landscape, the well-established Haber-Bosch method is employed for the catalytic synthesis of ammonia (NH_3) from hydrogen and nitrogen gases, necessitating elevated temperatures (400–600 ℃) and high pressures (150–300 atm, 1 atm= 0.101325 MPa). In response to the imperative to reduce energy consumption and environment impact imposed by this synthetic process, significant research efforts have converged on realizing NH_3 synthesis under ambient conditions. This study delves into the realm of N_2 electrocatalytic reduction to NH_3, using density functional theory (DFT) calculations to explore the feasibility of employing graphene co-doped with a combination of transition metal elements (*e.g.*, Fe, Nb, Mo, W, and Ru) and non-metal elements (*e.g.*, B, P, and S) as catalyst for ammonia synthesis. The findings underscore that Mo and S co-doped graphene (Mo/S graphene) demonstrates an exceptionally low electrode potential of 0.47 V for NH_3 synthesis, with the key rate-controlling step centered around the formation of the intermediate *NNH. Especially, the ammonia synthesis potential is found to be lower than the hydrogen evolution potential (0.51 V), conclusively affirming the selectivity of nitrogen reduction to ammonia. Furthermore, through *ab initio* molecular dynamics calculations, the study attests to the remarkable thermodynamic stability of the Mo/S co-doped graphene system under room temperature conditions. Notably, electronic structure analysis validates that the ability of electron communication of the transition metal plays a pivotal role in dictating the efficiency of N_2 electrocatalytic reduction. It can be tactically optimized through controlled modulation of the influence of the non-metal element on the coordination environment of the transition metal, thus substantially enhancing catalytic performance.

Key words: nitrogen reduction reaction; density functional theory; graphene; thermodynamic; electrocatalysis

Ammonia holds a significant role as both a vital industrial chemical and a promising sustainable fuel source due to its impressive gravimetric hydrogen density, reaching 17.75% (in mass)[1-3]. This prevailing industrial approach for ammonia production is the Haber-Bosch method, employing an iron-based catalyst and operating at high temperature (400–600 ℃) and high pressure (150–300 atm). Regrettably, this process accounts for a substantial 1%–2% of global energy consumption and contributes to 1.44% of worldwide CO_2 emission[4-8]. The urgent need to reduce energy consumption and mitigate environmental impact necessitates the exploration of alternative ammonia production methods. In theory, this could be realized by consecutive protonation steps under an applied potential, bypassing the direct cleavage of robust N≡N bonds. However, this requires the development of highly efficient catalysts capable of enhancing the nitrogen reduction reaction, a pursuit that has sparked tremendous enthusiasm.

Prior researches have highlighted functional graphene as a promising candidate for enhancing ammonia production

Received date: 2023-09-21; **Revised date:** 2023-11-22; **Published online:**2024-01-31
Foundation item: 上海市自然科学基金面上项目(21ZR1472900, 22ZR1471600)
Natural Science Foundation of Shanghai (21ZR1472900, 22ZR1471600)
Biography: LI Honglan (1983–), female, PhD candidate. E-mail: openfoam@just.edu.cn
李红兰(1983–), 女, 博士研究生. E-mail: openfoam@just.edu.cn
Corresponding author: SONG Erhong, associate professor. E-mail: ehsong@mail.sic.ac.cn; YANG Xinglin, professor. E-mail: hcyangxl2010@163.com
宋二红, 副研究员 E-mail: ehsong@mail.sic.ac.cn; 杨兴林, 教授. E-mail: hcyangxl2010@163.com

efficiency[9-11]. For instance, the introduction of molybdenum (Mo) as a dopant has been explored by Zhao *et al*.[12], who reported a limiting potential of 0.49 V for Mo/N_3-embedded graphene. Similarly, Ma *et al*.[13] found a thermodynamic barrier of 0.67 eV for Mo/N_4-embedded graphene along the distal reaction mechanism. While, Choi and colleagues[14] noted limiting potential of 0.89 V for Mo/C_3 and 0.69 V for Mo/C_4-embedded graphene, respectively. In our previous work[15], it was identified that Mo/C_6-embedded graphene presented a thermodynamic barrier of 0.37 eV. These results indicate that Mo, characterized by its partially-filled *d* band, strikes a delicate balance between reactant activation and potential intermediate inhibition. Furthermore, the variations in the reported limiting potentials hint at the influence of the metal center's reactivity modulation by its coordination environment. This concept gains further support from a study conducted by Zhou *et al*.[16], who introduced selenium (Se) heteroatom into Mo-doped graphene and observed a reduced limiting potential of 0.41 V for Mo/C_2Se-embedded graphene. Given the distinct electronic configurations of *p*-block elements, it is reasonable to anticipate that Mo's reactivity in ammonia synthesis depends on the specific *p*-block elements that it coordinated with. Our previous work has demonstrated that graphene's three-vacancy defects create sufficient space for the inclusion of *p*-block heteroatoms around the metal site[15]. Therefore, a crucial question arises regarding the impact of *p*-block heteroatoms on the catalytic performance of N_2-to-NH_3 conversion.

To address this question, our study investigated the influence of secondary *p*-block dopants (X = B, P, or S) on the electrocatalytic conversion of N_2 to NH_3 in TM/C_6-embedded graphene. The transition metals (TM) included Fe, Nb, Mo, Ru, and W. Herein, the selection of B, P, or S stemed from the previous reports[17-19]. Wherein, B and P are identified as the active sites to boost nitrogen reduction reaction (NRR), meanwhile S is a coordination element found in azotobacter, and the selection of Fe, Nb, Mo, Ru, and W is due to their reported good nitrogen-fixation activity[12,15,20-25]. Density functional theory (DFT) calculations were employed to evaluate the activity and selectivity by analyzing free energy profiles. We also assessed structural stability through binding energy and structural rigidity at room temperature. Furthermore, Mulliken charges and partial density of states were calculated to analyze the electronic structure and determine the extent to which the reactivity of the metal center is modulated by coordination with *p*-block heteroatoms.

1 Computational methods

We conducted all DFT calculations for the geometric optimizations and electronic properties using the DMol^3 software package[26-27]. The Perdew-Burke- Ernzerh (PBE) functional with generalized gradient approximation (GGA) was employed to describe the exchange-correlation effect[28]. To account for relative effects, the DFT Semi-core Pseudopots (DSPP) core treat method was used, which replaces core electrons with a single effective potential[29]. The double numerical atomic orbital augmented by a polarization function (DNP) was chosen as the basis set[26]. To achieve accurate electronic convergence, a smearing of 0.005 Ha (1 Ha = 27.21 eV) was applied to the orbital occupation. Structure optimization was performed until convergence critera were met, with an energy, maximum force and maximum displacement of 1.0×10^{-5} Ha, 0.02 Ha/nm and 0.0005 nm, respectively. For all calculations, the spin-unrestricted method was used. Additionally, a conductor-like screening model (COSMO) was employed to simulate a solvent environment resembling H_2O[30]. COSMO is a continuum model where the solute molecule creates a cavity within the dielectric continuum. We extended the DMol^3/COSMO method to accommodate periodic boundary conditions. The dielectric constant of H_2O was set as 78.54. The *ab initio* molecular dynamic (AIMD) simulations were conducted within the NVE ensemble to check the structural stability at room temperature.

(5×5) supercell was adopted to model the graphene monolayer consisting of 50 C atoms and the functional graphene was created *via* replacing three C atoms by one TM atom and one C atom by one X atom. To prevent artificial interactions between the catalyst and its images, a 1.5 nm thick vacuum was introduced. The adsorption energy, E_{ads}, of the NRR intermediate was calculated as follow:

$$E_{ads} = E_{system} - E_{catalyst} - E_m \quad (1)$$

Here, E_{system}, $E_{catalyst}$, and E_m represent the total energies of the adsorption system, the catalyst, and the adsorbates, respectively.

To access the thermodynamic stability of functional graphene, we calculated binding energy, E_b, using the following formula, widely used in the literature[31]:

$$E_b = E_{catalyst} - E_{XG} - E_{TM} \quad (2)$$

Where E_{XG} is the energy of graphene doped with non-metal atoms, and E_{TM} is the total energy of the transition metal atoms.

The Gibbs free energy change (ΔG) of the elementary steps was determined based on the CHE

model developed by Nørskov *et al*.[32] , where the chemical potential of the ($H^+ + e^-$) pair in solution equals half that of gas-phase H_2[32-33]. The corresponding ΔG was calculated as follow:

$$\Delta G = \Delta E + \Delta E_{ZPE} - T\Delta S + \Delta G_U + \Delta G_{pH} \quad (3)$$

Here, ΔE represents the energy difference, ΔE_{ZPE} is the change in zero point energy, and ΔS is the entropy change. The temperature, T, was set as 298.15 K. E_{ZPE} and S were determined from vibrational frequencies using standard methods. To simplify calculations, the substrates were fully constrained, following the suggestion of Wilcox *et al*.[34]. The term $\Delta G_U = -eU$ accounts for the free energy contribution caused due to variation in electrode potential U, while ΔG_{pH} is the pH correction of the free energy, equal to $kT\ln10 \times$ pH, with k representing the Boltzmann constant. In this case, the solution is acidic with a pH of zero. $\Delta G < 0$ indicates exothermic adsorption and *vice versa*. These methods have previously proven successfully in analyzing the N_2 fixation process, demonstrating their robustness and feasibility[14,35].

The limiting potential U_L is given by:

$$U_L = \Delta G_{PDS}/e \quad (4)$$

Where ΔG_{PDS} is the free energy change of the elementary step with the maximum endothermic character during the N_2-to-NH_3 conversion.

2　Results and discussion

Fig. 1(a) illustrates the structural model of TMX doped graphene. Fig. 1(b) shows the bond lengths, l_{TMX}, of TM–X bonds after geometrical optimization. Wherein, l_{TMB} is the shortest while l_{TMP} and l_{TMS} are similar in magnitude. For example, the l_{TMX} values are 2.108, 2.359 and 2.331 Å (1 Å = 10^{-10} m) for Mo–B, Mo–P and Mo–S bonds, respectively. To further characterize the TM–X interaction, Fig. 1(c) shows the binding energies, $E_{b(TMX)}$, between TM and its coordination atom. It reveals that $E_{b(TMS)}$ is the weakest while $E_{b(TMB)}$ is similar to $E_{b(TMP)}$. For example, $E_{b(TMX)}$ are −6.71, −6.95 and −5.80 eV for the MoB, MoP and MoS doped graphene, respectively. The disparity in $E_{b(TMX)}$ stems from valence electron configurations ($2s^22p^1$ for B, $3s^23p^3$ for P and $3s^23p^4$ for S). Due to lone pair, the S prefers to form two bonds with its coordination environment, for example S at the edge of graphene; however, it is different for B and P, which prefer to form three bonds with its coordination environment[36]. The presence of lone pair in the p band of S leads to the weakened $E_{b(TMS)}$, regardless of TM selection. As known, a high E_b represents strong chemical interaction, indicating that the metallic atom is firmly embedded into the graphene[20]. To further investigate the origin of the E_b differences, the partial density of states (PDOS) between the d band of Mo and the p band of X is shown in Fig. 1(d). The existence of pd coupling below the Fermi energy level confirms the formation of the Mo–X covalent bond. Furthermore, the reduced pd hybridization of the Mo–S bond is consistent with the weakened $E_{b(MoS)}$ value. Furthermore, the introduction of X into graphene also changes the d band distribution of Mo. The d band center, ε_d, is used to quantify this variation. Herein, the corresponding values are −1.54, −1.93 and −1.82 eV for MoB, MoP and MoS, respectively. A similar trend is observed for the rest TMX systems. The ε_d data are listed in Table S1 in Supporting Materials. With exception of FeX system, it is general tendency that ε_d of TMS is in the medium. However, $E_{b(TMS)}$ is always the weakest. Clearly, ε_d and E_b do not have the same trend. To shed the lights for the mentioned observations, we further analyzed the charge distribution and the Mulliken charge Q is also tabulated in Table S1 in Supporting Materials. As we known, one assumption of d band theory is that there is no electron change or electron filling of one element is fixed[37]. However, it is different from our case that Mulliken charge of TM is varied. Therefore, it is one reason that d band center ε_d could not describe the tendency of $E_{b(TMX)}$. Another possible reason is from the structural flexibility. The binding energy E_b is a sum of interaction energy E_{int} and deformation energy E_{def}. As shown in Table S2 in Supporting Materials, the E_{def} changes from 1.23 eV to 3.37 eV, indicating the structural deformation, which may raise the different trend. Herein, it is clear that the secondary dopant X is expected to change the TM reactivity.

Next, the adsorption behavior of the nitrogen molecule on graphene is considered. Fig. 2(a) illustrates the different adsorption structures, with aN_2 and bN_2 referring to the end-on and side-on N_2 adsorption, respectively, on the side of graphene with TM protrusion, while cN_2 and dN_2 stand for the corresponding adsorptions on the side of graphene with X protrusion. Fig. 2(b) shows the difference in adsorption free energy between N_2 molecules and H atoms, *i.e.* $\Delta\Delta G_{ads} = G_{ads}(*N_2) - G_{ads}(*H)$, as a function of the free energy of nitrogen adsorption, $G_{ads}(*N_2)$, for the different structures. Possessing a good affinity toward nitrogen and a relatively weak hydrogen adsorption are prerequisite for improving the selectivity of NRR *vs* hydrogen evolution reaction (HER). Therefore, a good catalyst should possess the properties of $G_{ads}(*N_2) < 0$ eV and $\Delta\Delta G_{ads} < 0$ eV[38]. Based on the $G_{ads}(*N_2)$, aN_2 is identified as the most stable configuration, and hence is the only initial state considered in the subsequent activity investigation. Then, the H adsorption on top site of TM

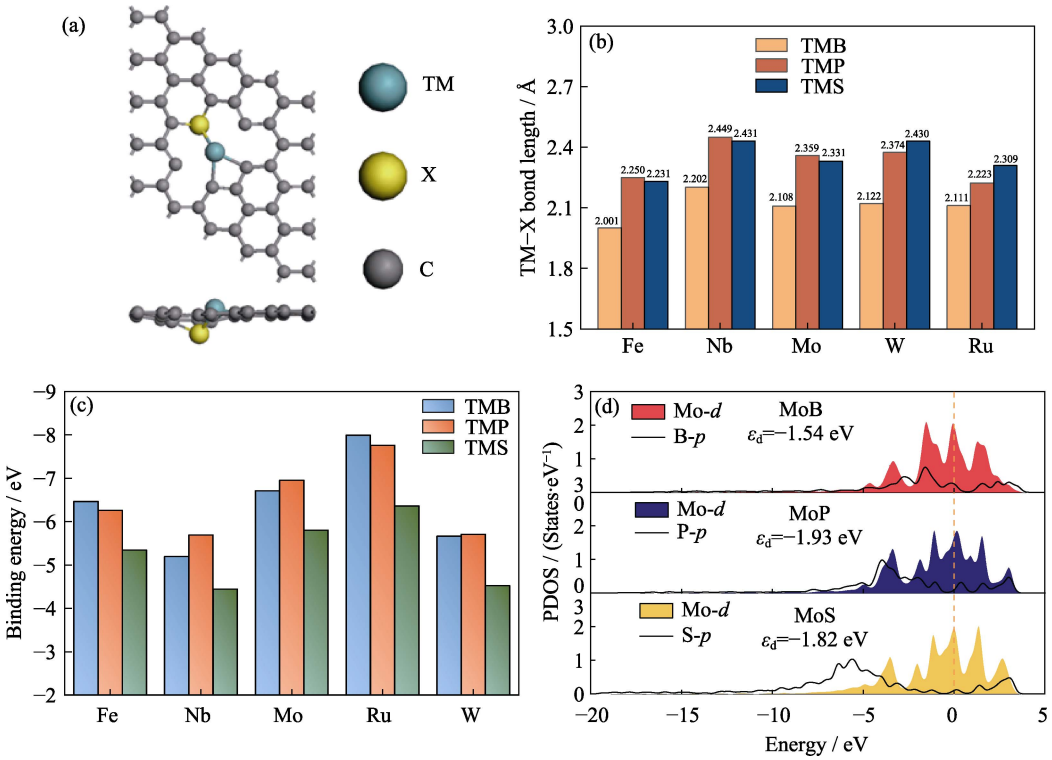

Fig. 1 Structure, optimized lengths, binding energy and partial density of states (PDOS)of TMX

(a) Atomic structure diagram of TMX doped graphene; (b) Optimized lengths, l_{TMB}, of the TM–X bonds; (c) Binding energy, $E_{b(TMX)}$, of TMX doped graphene; (d) PDOS between the *d* band of Mo and the *p* band of X for MoX doped graphene; Colorful figures are available on website

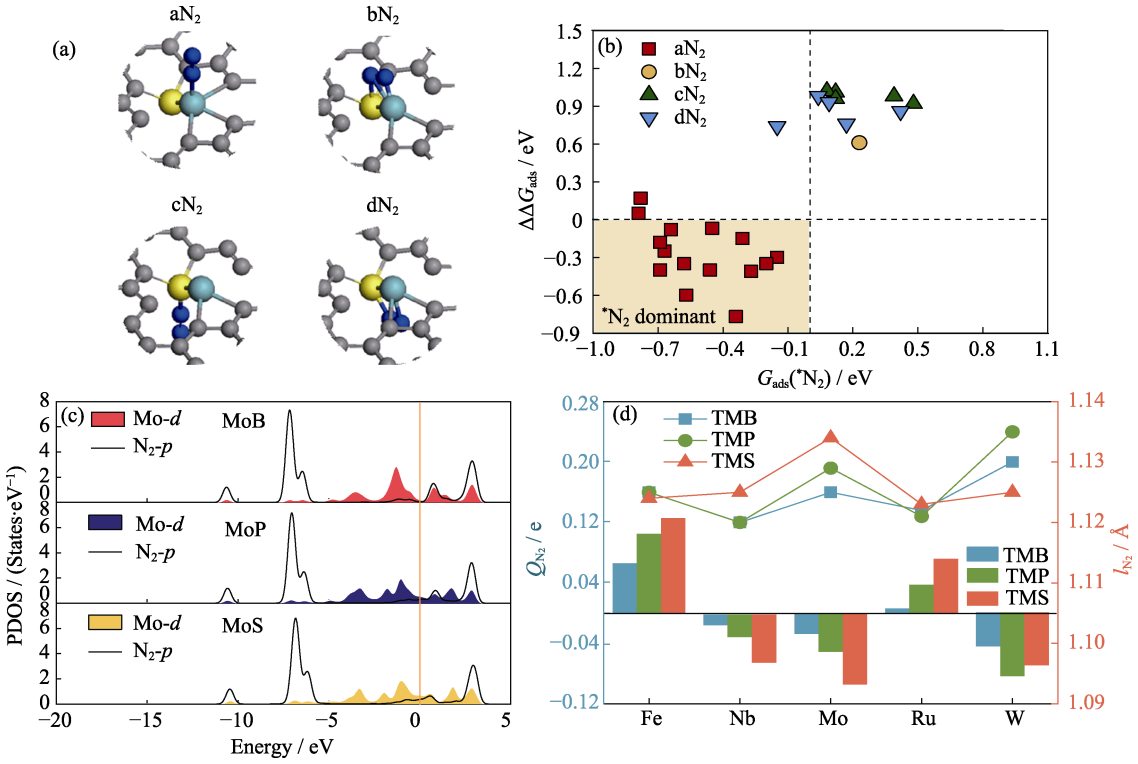

Fig. 2 Adsorption behavior of the nitrogen molecule on graphene

(a) Schematic diagram of N_2 adsorption structures; (b) Difference in the adsorption free energy of N_2 and H, $\Delta\Delta G_{ads}$= G_{ads}(*N_2)–G_{ads}(*H), as a function of G_{ads}(*N_2); (c) PDOS between the *d* band of Mo and the *p* band of N_2 for MoB, MoP, and MoS doped graphene; (d) Charge, Q_{N_2}, and bond length, l_{N_2}, of the N_2 adsorbate; Colorful figures are available on website

atom was considered, which is the same as aN_2 adsorption, in order to reveal the competition of reactant adsorption. After optimization, H is still located at the top site of TM atom with only exception of FeB wherein H adsorption is on bridge site between Fe atom and B atom. The corresponding adsorption structures are shown in Fig. S1 in Supporting Materials. From $\Delta\Delta G_{ads}$ values, H adsorption is energetically favorable on WP and WS while N_2 adsorption is favored on the rest systems. To further investigate the N_2 adsorption, Fig. 2(c) shows the PDOS between the *p* band of adsorbed N_2 and the *d* band of Mo as a representative system. It is evident that there is orbital hybridization around the Fermi energy level, which is consistent with the negative G_{ads}(*N_2). Additionally, electron occupation in the Fermi energy level is beneficial for electron communication upon adsorption. To quantitatively describe the activation of the N_2 adsorbate, its Mulliken charge, Q_{N_2}, and bond length, l_{N_2}, are shown in Fig. 2(d). The results show that the N_2 adsorbate is negatively charged on the MoX, NbX, and WX systems. Due to electron accumulation, the value of l_{N_2} increases from its original (unadsorbed) value of 1.108 Å to above 1.120 Å, indicating weakened N≡N bonds. Hence, this data validates the activation of N_2 on these systems. Furthermore, electron accumulation on the N_2 adsorbate is crucial for triggering the subsequent protonation progress due to electrostatic attraction between the negatively charged N_2 adsorbate and positively charged H^+. However, the N_2 adsorbate is positively charged on FeX and RuX systems, implying insufficient N_2 activation.

After establishing the catalyst structure and adsorption properties, a complete study of the NRR was conducted. Due to the energetic preference of N_2 adsorption in an end-on manner, the feasible reactions are *via* the distal and alternative pathways, not the enzymatic pathway[17,39-40]. This means that the proton-electron pairs will either continuously attack one N atom until NH_3 is formed or alternately attack two N atoms and thereby produce two NH_3 molecules simultaneously. What is more, we did not consider the direct splitting pathway, which is generally infeasible for single-active site. Taken MoX as an example, optimization calculations on the adsorption structures consisting of two N atoms co-adsorption on Mo top site were performed. After optimization, two N atoms adsorbed at MoB and MoS systems would spontaneously combine together to form N_2, and the co-adsorption of two N atoms is only possible for MoP system. Then the calculation of TS search was conducted to identify the kinetic barrier of N_2 splitting catalyzed by MoP moiety. As shown in Fig. S2 in Supporting Materials, the reaction barrier is about 3.91 eV. The extra-high barrier in combination with the endothermic reaction energy means the impossibility for direct N_2 splitting. Therefore, we considered the distal and alternative pathways in the following discussions.

Taking MoS as an example, Fig. 3(a, b) describe the free energy profiles under the distal and alternative

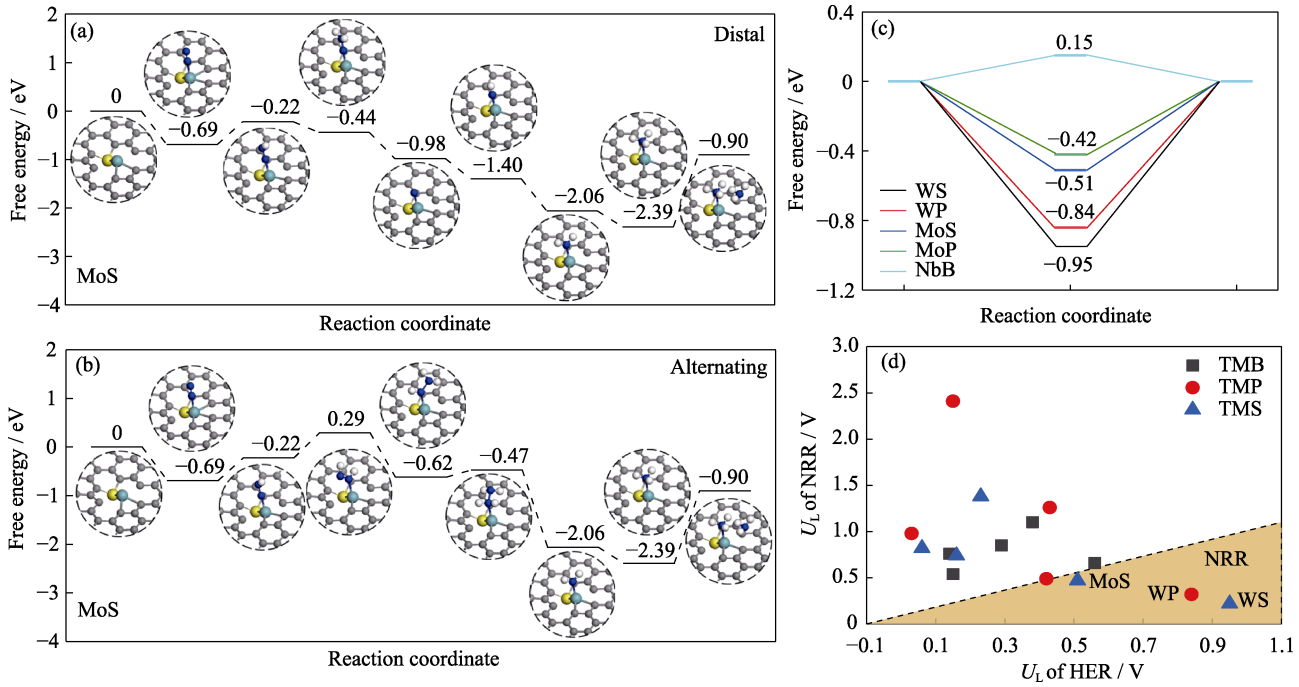

Fig. 3　Free energy and plotting U_L(NRR) *vs* U_L(HER) of the catalysts

(a, b) Free energy profiles for NRR of MoS doped graphene *via* (a) distal pathway and (b) alternating pathway; (c) Free energy profiles for HER of WS, WP, MoS, MoP, and NbB doped graphene; (d) Comparison between limiting potential of NRR and reduction potential of HER; Colorful figures are available on website

pathways, respectively. For the former, ΔG of the elementary (consecutive) protonation steps are 0.47, –0.22, –0.54, –0.42, –0.66, –0.33, and 1.49 eV, respectively. Therefore, the potential-determining step (PDS) along the distal pathway is the first protonation step, *i.e.* $N_2 + H^+ + e^- \rightarrow$ *NNH, and its corresponding thermodynamic barrier, ΔG_{PDS}, is 0.47 eV. For the alternating pathway, the corresponding ΔG are 0.47, 0.51, –0.91, 0.15, –1.59, –0.33, and 1.49 eV, respectively. In this case, the PDS is the second protonation step, *i.e.* *NNH + H^+ + e^-→ *NHNH, and ΔG_{PDS} is 0.51 eV. Hence, the distal pathway is slightly preferred under the limiting potential, U_L(NRR), of 0.47 V. Following a similar analysis, ΔG and U_L(NRR) for all TMX systems are summarized in Table S3 in Supporting Materials. The lower U_L(NRR), the less energy is required to catalyze the reaction, indicating higher activity. Generally, a U_L(NRR) less than 0.55 V indicates good reactivity toward nitrogen fixation. Using this criterion, WS, WP, MoS, MoP, and NbB are expected to be active, with U_L(NRR) of 0.22, 0.32, 0.47, 0.49, and 0.54 V, respectively, and their activities are in the order of WS > WP > MoS ≈ MoP ≈ NbB. The rest systems considered are not very reactive for ammonia synthesis due to their relatively high U_L(NRR), which is consistent with the Q_{N_2} analysis.

As HER is the main side reaction, which directly consumes protons and electrons meant for NRR[14,41-42], the selectivity of NRR *vs* HER was studied further *via* a comparison of limiting potentials. Fig. 3(c) shows the HER free energy profiles of WS, WP, MoS, MoP, and NbB systems. For WS, WP, MoS, and MoP, the first protonation step is exothermic while the second protonation step is endothermic, indicating that hydrogen evolution suffers from too strong H adsorption. As shown in Fig. 3(c), the decoration of X heteroatoms influences the HER performance, resulting in U_L(HER) values of 0.95, 0.84, 0.42 and 0.51 V for WS, WP, MoP and MoS, respectively. By contrast, the proton capture step on NbB is endothermic, and the HER occurs under a U_L(HER) of 0.15 V. Plotting U_L (NRR) *vs* U_L(HER) in Fig. 3(d) shows that WS, WP, and MoS are active for ammonia synthesis; however, the efficiencies of N_2-to-NH_3 conversion on MoP and NbB are limited by the undesirable HER. Furthermore, it should be noted that, as mentioned earlier, the positive $\Delta\Delta G_{ads}$ for WS and WP demonstrate that the H adsorption on these catalysts is stronger than N_2 adsorption, which implies that the active sites are inaccessible for N_2 molecules due to being covered by protons. Therefore, MoS appears to be the only promising candidate for nitrogen fixation electrocatalysis.

From the mentioned results, it is clear that the introduction of *p*-block heteroatoms influences the reactivity of the metal center in the application of N_2-to-NH_3 conversion. In order to further reveal the physical origin of this effect, Mulliken charge population analysis of MoX systems during the consecutive protonation progress was performed. According to previous report[17], each intermediate is divided into three

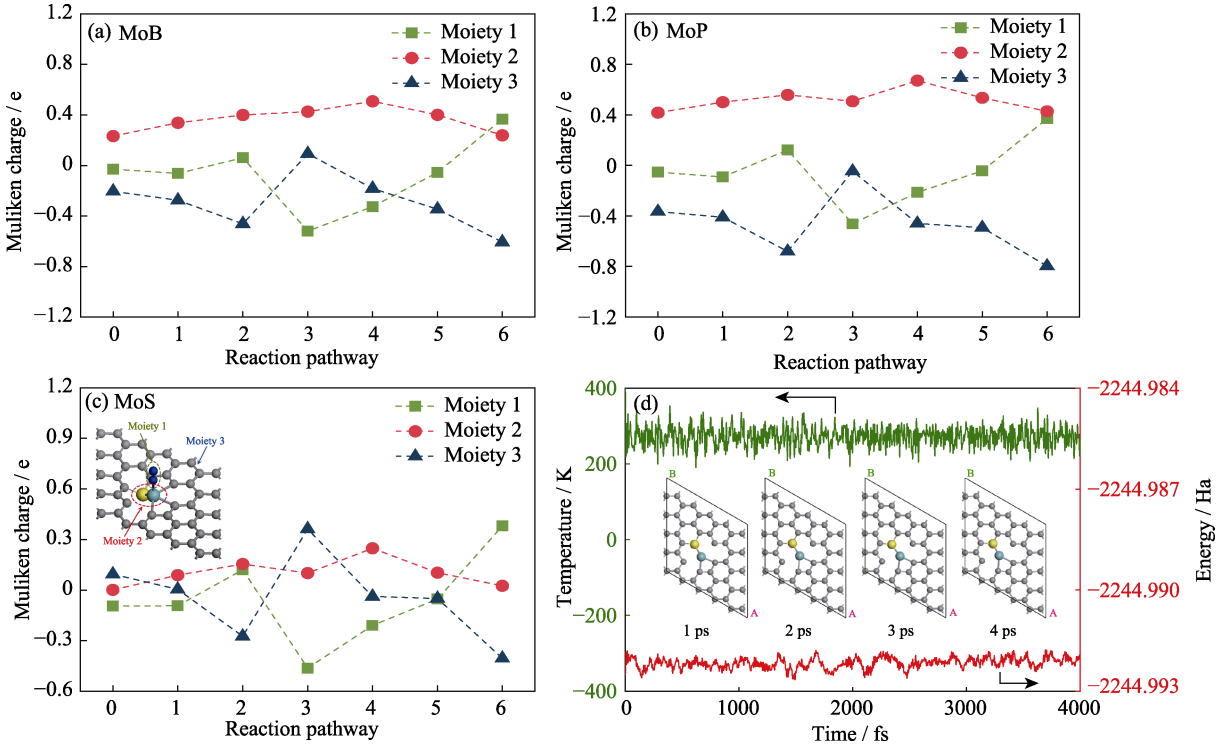

Fig. 4 Variation of Mulliken charge and energy of the catalysts

(a-c) Mulliken charge variation of (a) MoB, (b) MoP, and (c) MoS *via* the distal pathway;

(d) Variation of temperature and energy of MoS during the AIMD simulation

moieties: N_xH_y adsorbates (moiety 1), MoX (moiety 2) and the graphene support (moiety 3). The results presented in Fig. 4(a-c) show electron communication between the graphene support and the intermediates, indicating effective electron transfer during protonation steps, which is consistent with previous studies[43-44]. Furthermore, the MoX moiety donates electrons to N_xH_y species, with MoS less positively charged compared with MoB and MoP. It demonstrates that the introduction of *p*-block heteroatoms influences the electrocatalysis of nitrogen reduction by affecting the electron transfer. To support the idea, we further plotted the fitting between the limiting potential $U_{L(NRR)}$ and the Mulliken charge $Q(N_2*)$ of the adsorbed N_2, as shown in Fig. S3 in Supporting Materials. Consistently, more charge accumulated in N_2 reactant, smaller $U_{L(NRR)}$ required for nitrogen reduction. Our results are in line with the reported electron acceptance-back donation mechanism[21,45]. Last but not least, AIMD simulation is preformed to check the structural robustness of MoS doped graphene. As shown in Fig. 4(d), its atomic structure is well-maintained at room temperature. Therefore, Mo/S co-doped graphene endowed with low limiting potential and good structural stability, holds feasibility in the application of ammonia synthesis electrocatalysis.

3 Conclusions

This study explores the potential of transition metal/non-metal co-doped graphene as electrocatalysts for ammonia synthesis through DFT calculations. Our findings indicate that W/S, W/P, Mo/S, Mo/P, and Nb/B exhibit promising activity with relatively low limiting potentials of 0.22, 0.32, 0.47, 0.49, and 0.54 V, respectively. Nevertheless, W/S, W/P, Mo/P, and Nb/B also enhance the side hydrogen evolution reaction, compromising ammonia synthesis selectivity. Consequently, Mo/S emerges as the most compelling candidate for experimental verification due to its remarkable efficiency and stability. Furthermore, our DFT calculations reveal that the metal center's reactivity can be finely tuned by coordinating with *p*-block heteroatoms, presenting novel prospects for ammonia synthesis.

Supporting Materials

The supporting materials related to this article can be found at https://doi.org/10.15541/jim20230433.

References:

[1] ROSCA V, DUCA M, DE GROOT M T, *et al.* Nitrogen cycle electrocatalysis. *Chemical Reviews*, 2009, **109(6):** 2209.

[2] ZHAO S L, LU X Y, WANG L Z, *et al.* Carbon-based metal-free catalysts for electrocatalytic reduction of nitrogen for synthesis of ammonia at ambient conditions. *Advanced Materials*, 2019, **31(13):** 1805369.

[3] ZHANG L, DING L, CHEN G, *et al.* Ammonia synthesis under ambient conditions: selective electroreduction of dinitrogen to ammonia on black phosphorus nanosheets. *Angewandte Chemie International Edition*, 2019, **58(9):** 2612.

[4] GUO W, ZHANG K, LIANG Z, *et al.* Electrochemical nitrogen fixation and utilization: theories, advanced catalyst materials and system design. *Chemical Society Reviews*, 2019, **48(24):** 5658.

[5] HUANG L S, GU X L, ZHENG G F. Tuning active sites of MXene for efficient electrocatalytic N_2 fixation. *Chem*, 2019, **5(1):** 15.

[6] LING C Y, ZHANG Y H, QIANG L, *et al.* New mechanism for N_2 reduction: the essential role of surface hydrogenation. *Journal of the American Chemical Society*, 2019, **141(45):** 18264.

[7] JIAO F, XU B. Electrochemical ammonia synthesis and ammonia fuel cells. *Advanced Materials*, 2019, **31(31):** 1805173.

[8] KITANO M, INOUE Y, YAMAZAKI Y, *et al.* Ammonia synthesis using a stable electride as an electron donor and reversible hydrogen store. *Nature Chemistry*, 2012, **4(11):** 934.

[9] LI J, CHEN S, QUAN F. Accelerated dinitrogen electroreduction to ammonia *via* interfacial polarization triggered by single-atom protrusions. *Chem*, 2020, **6(4):** 885.

[10] XI J, JUNG H S, XU Y, *et al.* Synthesis strategies, catalytic applications, and performance regulation of single-atom catalysts. *Advanced Functional Materials*, 2021, **31(12):** 2008318.

[11] SHREYA M, YANG X X, SHAN W T, *et al.* Atomically dispersed single Ni site catalysts for nitrogen reduction toward electrochemical ammonia synthesis using N_2 and H_2O. *Small Methods*, 2020, **4(6):** 1900821.

[12] ZHAO W H, CHEN L L, ZHANG W H, *et al.* Single $Mo_1(W_1, Re_1)$ atoms anchored in pyrrolic-N_3 doped graphene as efficient electrocatalysts for the nitrogen reduction reaction. *Journal of Materials Chemistry A*, 2021, **9(10):** 6547.

[13] YANG Y, LIU J, WEI Z, *et al.* Transition metal-dinitrogen complex embedded graphene for nitrogen reduction reaction. *ChemCatChem*, 2019, **11(12):** 2821.

[14] CHOI C, BACK S, KIM.N Y, *et al.* Suppression of hydrogen evolution reaction in electrochemical N_2 reduction using single-atom catalysts: a computational guideline. *ACS Catalysis*, 2018, **8(8):** 7517.

[15] WU J, YANG L, LIU X, *et al.* ZrN_6-doped graphene for ammonia synthesis: a density functional theory study. *ChemPhysChem*, 2022, **24(8):** e202200864.

[16] ZHOU H Y, LI J C, WEN Z, *et al.* Tuning the catalytic activity of a single Mo atom supported on graphene for nitrogen reduction *via* Se atom doping. *Physical Chemistry Chemical Physics*, 2019, **21(27):** 14583.

[17] LIU C, LI Q, WU C, *et al.* Single-boron catalysts for nitrogen reduction reaction. *Journal of the American Chemical Society*, 2019, **141(7):** 2884.

[18] ZHAO Z M, LONG Y, CHEN Y, *et al.* Phosphorus doped carbon nitride with rich nitrogen vacancy to enhance the electrocatalytic activity for nitrogen reduction reaction. *Chemical Engineering Journal*, 2021, **430(1):** 132682.

[19] LI.Q Y, QIU S Y, LIU C G, *et al.* Computational design of single-molybdenum catalysts for the nitrogen reduction reaction. *Journal of Physical Chemistry C*, 2019, **123(4):** 2347.

[20] ZHANG S, WANG M, JIANG S, *et al.* The activation and reduction of N_2 by single/double-atom electrocatalysts: a first-principle study. *ChemistrySelect*, 2021, **6(8):** 1787.

[21] WU J, YANG L, LIU X, *et al.* Transition metal decorated bismuthene for ammonia synthesis: a density functional theory study. *Chinese Chemical Letters*, 2022, **34(6):** 107659.

[22] CHEN Z, ZHAO J X, CABRERA C R, *et al.* Computational screening of efficient single-atom catalysts based on graphitic carbon nitride (g-C_3N_4) for nitrogen electroreduction. *Small Methods*, 2018, **3(6):** 1800368.

[23] LIU K, FU J W, ZHU L, *et al.* Single-atom transition metals supported on black phosphorene for electrochemical nitrogen

reduction. *Nanoscale*, 2020, **12(8):** 4903.
[24] XU Z W, SONG R F, WANG M Y, *et al.* Single atom-doped arsenene as electrocatalyst for reducing nitrogen to ammonia: a DFT study. *Physical Chemistry Chemical Physics*, 2020, **22(45):** 26223.
[25] SONG R F, YANGJ, WANG M Y, *et al.* Theoretical study on P-coordinated metal atoms embedded in arsenene for the conversion of nitrogen to ammonia. *ACS Omega*, 2021, **6(12):** 8662.
[26] DELLEY B. An all-electron numerical method for solving the local density functional for polyatomic molecules. *Journal of Chemical Physics,* 1990, **92(1):** 508.
[27] DELLEY B. From molecules to solids with the $DMol^3$ approach. *Journal of Chemical Physics*, 2000, **113(18):** 7756.
[28] PERDEW J P, BURKE K, ERNZERHOF M. Generalized gradient approximation made simple. *Physical Review Letters*, 1996, **77(18):** 3865.
[29] DELLEY B. Hardness conserving semilocal pseudopotentials. *Physical Review B*, 2002, **66(15):** 155125.
[30] TODOROVA T, DELLEY B. Wetting of paracetamol surfaces studied by $DMol^3$-COSMO calculations. *Molecular Simulation*, 2008, **34(10):** 1013.
[31] CUI C N, ZHANG H C, LUO Z X. Nitrogen reduction reaction on small iron clusters supported by N-doped graphene: a theoretical study of the atomically precise active-site mechanism. *Nano Research*, 2020, **13(8):** 2280.
[32] NØRSKOV J K, ROSSMEISL J. Origin of the overpotential for oxygen reduction at a fuel-cell cathode. *Journal of Physical Chemistry B*, 2004, **108(46):** 17886.
[33] AMBARISH K, SAMIRA S, ANJLI P, *et al.* Understanding catalytic activity trends in the oxygen reduction reaction. *Chemical Reviews*, 2018, **118(5):** 2302.
[34] LIM D H, WILCOX J. Mechanisms of the oxygen reduction reaction on defective graphene-supported Pt nanoparticles from first-principles. *Journal of Physical Chemistry C*, 2012, **116(5):** 3653.
[35] ZHAO J X, CHEN Z F. Single Mo atom supported on defective boron nitride monolayer as an efficient electrocatalyst for nitrogen fixation: a computational study. *Journal of the American Chemical Society*, 2017, **139(36):** 12480.
[36] JIAO Y, ZHENG Y, DAVEY K, *et al.* Activity origin and catalyst design principles for electrocatalytic hydrogen evolution on heteroatom-doped graphene. *Nature Energy*, 2016, **1:** 16130.
[37] HAMMER B, NØRSKOV J K. Theoretical surface science and catalysis—calculations and concepts. *Advances in Catalysis,* 2000, **45:** 71.
[38] LIU X, CHENG Y J, ZHENG Y, *et al.* Building up a picture of the electrocatalytic nitrogen reduction activity of transition metal single atom catalysts. *Journal of the American Chemical Society*, 2019, **141(24):** 9664.
[39] WEI Z X, ZHANG Y F, WANG S Y, *et al.* Fe-doped phosphorene for the nitrogen reduction reaction. *Journal of Materials Chemistry A*, 2018, **6(28):** 13790.
[40] SONG W, WANG J, FU L, *et al.* First-principles study on Fe_2B_2 as efficient catalyst for nitrogen reduction reaction. *Chinese Chemical Letters*, 2021, **32(10):** 3137.
[41] AAYUSH R S, BRIAN A R, JAY A S, *et al.* Electrochemical ammonia synthesis—the selectivity challenge. *ACS Catalysis*, 2016, **7(1):** 706.
[42] LIU C W, LI Q Y, ZHANG J, *et al.* Theoretical evaluation of possible 2D boron monolayer in N_2 electrochemical conversion into ammonia. *Journal of Physical Chemistry C*, 2018, **122(44):** 25268.
[43] XIAO B B, YANG L, YU L B, *et al.* The VN_3 embedded graphane with the improved selectivity for nitrogen fixation. *Applied Surface Science*, 2020, **513(30):** 145855.
[44] WANG Z G, WU H H, LI Q, *et al.* Reversing interfacial catalysis of ambipolar WSe_2 single crystal. *Advanced Science*, 2019, **7(3):** 1901382.
[45] LIU X, YANG L, WEI T, *et al.* Active MoS_2-based electrode for green ammonia synthesis. *Chinese Journal of Chemical Engineering*, 2023, **65:** 268.

Mo/S 共掺杂的石墨烯用于合成氨：密度泛函理论研究

李红兰[1], 张俊苗[1], 宋二红[2], 杨兴林[1]

(1. 江苏科技大学 能源与动力学院, 镇江 212003; 2. 中国科学院 上海硅酸盐研究所, 高性能陶瓷和超微结构国家重点实验室, 上海 200050)

摘 要: 工业界普遍采用 Haber-Bosch 方法在高温(400~600 ℃)和高压(150~300 atm, 1 atm= 0.101325 MPa)条件下催化氮气裂解和加氢而合成氨气(NH_3), 这不仅消耗大量能源, 也给环境造成很大污染。为改变这种状况, 探索常温常压条件下合成 NH_3 的全新途径已成为研究热点。电催化还原 N_2 合成 NH_3 是尚待探索的重点方向之一。本研究利用密度泛函理论计算, 探讨了过渡金属元素(如 Fe, Nb, Mo, W, Ru)和非金属元素(如 B, P, S)共掺杂石墨烯作为该方向催化剂的可行性。结果表明, Mo 和 S(Mo/S)共掺杂石墨烯在 NH_3 合成中具有极低的电极电势(仅为 0.47 V), 其速率控制步骤涉及的中间产物为*NNH。NH_3 合成电势比析氢反应的电势(0.51 V)低, 说明 N_2 还原制备 NH_3 具有选择性。经从头算的分子动力学计算验证, Mo/S 共掺杂石墨烯体系在室温下具有良好的热力学稳定性。电子结构分析进一步揭示, 过渡金属电子转移能力对高效 N_2 电催化还原活性具有关键影响, 可通过调控非金属元素对过渡金属周边配位环境的影响, 优化过渡金属中心的电子结构, 从而提高催化性能。

关 键 词:氮气还原反应; 密度泛函理论; 石墨烯; 热力学; 电催化

中图分类号: TQ174 **文献标志码:** A **文章编号:** 1000-324X(2024)05-0561-08

Supporting Materials:

Mo/S Co-doped Graphene for Ammonia Synthesis: a Density Functional Theory Study

LI Honglan[1], ZHANG Junmiao[1], SONG Erhong[2], YANG Xinglin[1]

(1. School of Energy and Power Engineering, Jiangsu University of Science and Technology, Zhenjiang 212003, China; 2. State Key Laboratory of High Performance Ceramics and Superfine Microstructure, Shanghai Institute of Ceramics, Chinese Academy of Sciences, Shanghai 200050, China)

Table S1　Mulliken charge Q (in e) of TM and X and the d band center ε_d (in eV) of TM in TMX-doped graphene

	Q_{TM}			Q_X			ε_d		
	B	P	S	B	P	S	B	P	S
Fe	–0.133	–0.015	0.061	0.172	0.427	–0.100	–1.007	–1.330	–1.383
Nb	0.566	0.486	0.628	0.123	0.437	–0.147	–1.489	–2.475	–2.157
Mo	0.234	0.147	0.267	0.188	0.479	–0.107	–1.556	–1.930	–1.820
Ru	–0.187	–0.207	–0.032	0.315	0.721	–0.046	–1.632	–2.078	–1.787
W	0.247	0.137	0.265	0.189	0.482	–0.108	–1.669	–2.135	–1.915

Table S2　Binding energy $E_{b(TMX)}$ (in eV), interaction energy E_{int} (in eV) and deformation energy E_{def} (in eV)

	B			P			S		
	E_b	E_{int}	E_{def}	E_b	E_{int}	E_{def}	E_b	E_{int}	E_{def}
Fe	–6.46	–8.69	2.23	–6.26	–7.49	1.23	–5.35	–6.58	1.23
Nb	–5.19	–8.06	2.86	–5.69	–8.42	2.73	–4.44	–7.36	2.92
Mo	–6.71	–9.83	3.12	–6.95	–9.95	2.99	–5.80	–8.89	3.09
Ru	–7.99	–10.09	2.09	–7.76	–9.40	1.64	–6.36	–7.94	1.58
W	–5.67	–9.04	3.37	–5.71	–8.96	3.26	–4.52	–7.89	3.37

Table S3　Free energy changes of protonation steps ΔG_i (i = 1,2, ⋯, 6). $G_{ads}(N_2)$ and $G_{ads}(H)$ are the free energy (in eV) of nitrogen and hydrogen adsorption, respectively. $U_{L(NRR)}$ and $U_{L(HER)}$ are the limiting potentials (in V) of the nitrogen reduction reaction (NRR) and hydrogen evolution reaction (HER), respectively

System	Pathway	$G_{ads}(N_2)$	ΔG_1	ΔG_2	ΔG_3	ΔG_4	ΔG_5	ΔG_6	$G_{ads}(H)$	$U_{L(NRR)}$	$U_{L(HER)}$
FeB	Distal	–0.45	0.27	–0.36	1.11	–2.22	–0.74	0.46	–0.38	0.81	0.38
	Alternating	–0.45	0.27	**0.81**	–1.38	0.58	–2.23	0.46			
FeP	Distal	–0.57	**0.98**	–0.35	0.60	–0.84	–1.28	–0.88	0.03	0.98	0.03
	Alternating	–0.57	0.98	0.15	2.42	–0.32	–4.12	–0.88			
FeS	Distal	–0.46	**0.82**	–0.25	0.67	–0.91	–1.36	–0.76	–0.06	0.82	0.06
	Alternating	–0.46	0.82	0.17	–0.52	–0.35	–1.16	–0.76			
NbB	Distal	–0.15	–1.99	–0.15	**0.54**	–1.63	–1.21	–0.53	0.15	0.54	0.15
	Alternating	–0.15	–1.99	–0.07	–0.59	–0.44	–1.36	–0.53			
NbP	Distal	–0.20	–2.00	**2.41**	0.57	–1.62	–0.81	–0.54	0.15	2.41	0.15
	Alternating	–0.20	–2.00	3.02	–0.75	–0.11	–1.63	–0.54			
NbS	Distal	–0.31	**0.74**	–0.50	0.39	–1.47	–0.78	–0.42	–0.16	0.74	0.16
	Alternating	–0.31	0.74	0.16	–0.69	–0.08	–1.74	–0.42			
MoB	Distal	–0.69	**0.85**	–0.39	0.01	–1.01	–0.80	–0.60	–0.29	0.85	0.29
	Alternating	–0.69	0.85	–0.04	–0.56	–0.31	–1.28	–0.60			
MoP	Distal	–0.67	**0.49**	–0.24	–0.41	–0.58	–0.65	–0.45	–0.42	0.49	0.42
	Alternating	–0.67	0.49	0.35	–0.79	0.03	–1.46	–0.45			
MoS	Distal	–0.69	**0.47**	–0.22	–0.54	–0.42	–0.67	–0.33	–0.51	0.47	0.51
	Alternating	–0.69	0.47	0.51	–0.90	0.14	–1.59	–0.33			
RuB	Distal	–0.27	**0.76**	0.20	–0.47	0.14	–1.22	–1.00	0.14	0.76	0.14
	Alternating	–0.27	0.76	0.52	–0.63	–0.37	–0.88	–1.00			
RuP	Distal	–0.34	**1.26**	–0.09	0.05	–0.53	–1.33	–0.92	0.43	1.26	0.43
	Alternating	–0.34	1.26	0.02	–0.19	–0.76	–0.97	–0.92			
RuS	Distal	–0.58	**1.38**	–0.55	0.32	–0.48	–1.36	–0.99	–0.23	1.38	0.23
	Alternating	–0.58	1.38	–0.24	–0.20	–0.70	–0.92	–0.99			
WB	Distal	–0.64	**0.66**	–0.49	–0.09	–1.06	–0.71	–0.25	–0.56	0.66	0.56
	Alternating	–0.64	0.66	0.07	–0.70	0.12	–1.84	–0.25			
WP	Distal	–0.79	**0.32**	–0.45	–0.35	–0.80	–0.45	–0.10	–0.84	0.32	0.84
	Alternating	–0.79	0.32	0.46	–0.84	0.34	–2.01	–0.10			
WS	Distal	–0.78	**0.22**	–0.33	–0.59	–0.62	–0.45	0.11	–0.95	0.22	0.95
	Alternating	–0.78	0.22	0.77	–1.07	0.47	–2.15	0.11			

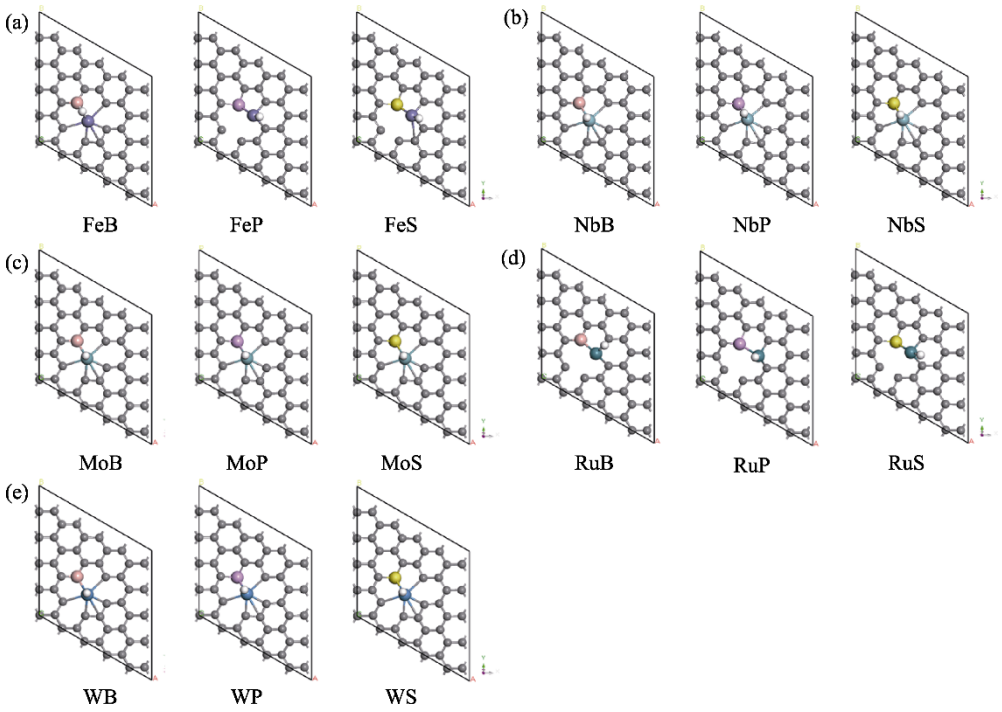

Fig. S1 H adsorption structures of (a) FeX, (b) NbX, (c) MoX, (d) RuX, and (e) WX

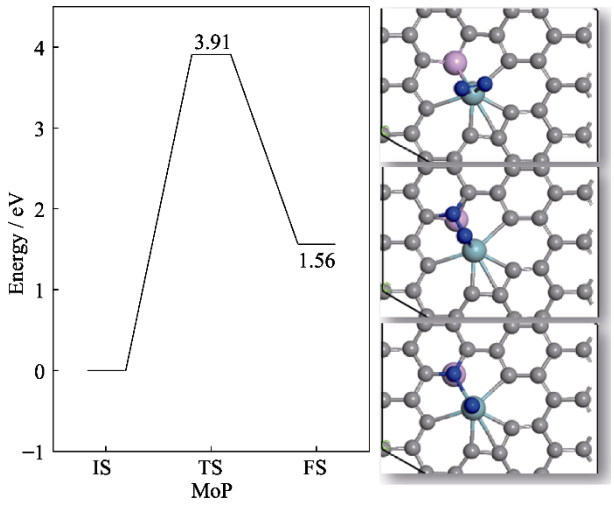

Fig. S2 Reaction coordinate of N_2 splitting catalyzed by MoP doped graphene
Right up: structure of initial state (IS); Right middle: structure of transition state (TS); Right down: structure of final state (FS)

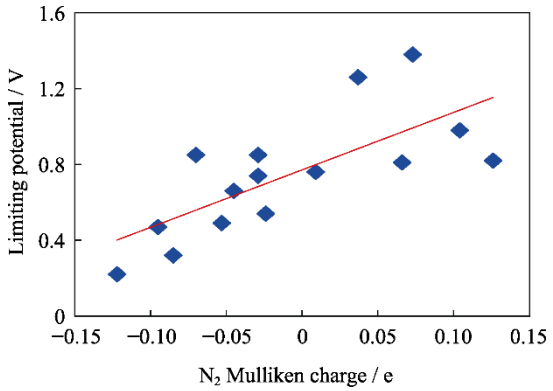

Fig. S3 Fitting between $U_{L(NRR)}$ and N_2* Mulliken charge $Q(N_2*)$ of TMX-doped graphene